Charge density waves in electron-doped molybdenum disulfide

Mohammed K. Bin Subhan,[†] Asif Suleman,[†,§] Gareth Moore,[†,§] Peter Phu,[†] Moritz Hoesch,[‡] Hidekazu Kurebayashi,[¶,‖] Christopher A. Howard,[*,†] and Steven R. Schofield[*,†,§]

[†]*Department of Physics and Astronomy, University College London, WC1E 6BT, London, UK*

[‡]*Photon Science, Deutsches Elektronen-Synchrotron (DESY), Notkestrasse 85, 22607 Hamburg, Germany*

[¶]*London Centre for Nanotechnology, University College London, WC1H 0AH, London, UK*

[§]*London Centre for Nanotechnology, University College London, WC1H 0AH, London, UK*

[‖]*Department of Electronic and Electrical Engineering, University College London, WC1E 6BT, London, UK*

E-mail: c.howard@ucl.ac.uk; s.schofield@ucl.ac.uk

June 30, 2021

Abstract

We present the discovery of a charge density wave (CDW) ground state in heavily electron-doped molybdenum disulfide (MoS_2). This is the first observation of a CDW in any d^2 (column 6) transition metal dichalcogenide (TMD). The band structure of MoS_2 is distinct from the d^0 and d^1 TMDs in which CDWs have been previously observed, facilitating new insight into CDW formation. We demonstrate a metal-insulator

1

transition at 85 K, a 25 meV gap at the Fermi level, and two distinct CDW modulations, $(2\sqrt{3} \times 2\sqrt{3})\text{R}30°$ and 2×2, attributable to Fermi surface nesting (FSN) and electron-phonon coupling (EPC), respectively. This simultaneous exhibition of FSN and EPC CDW modulations is unique among observations of CDW ground states, and we discuss this in the context of band folding. Our observations provide a route toward the resolution of controversies surrounding the origin of CDW modulations in TMDs.

Keywords: Charge density wave, metal-insulator transition, MoS_2, intercalation, STM, tunnelling spectroscopy.

Strongly anisotropic crystals that confine charge carriers to two-dimensions (2D) exhibit a rich diversity of correlated ground states, including charge density waves (CDWs), spin density waves, and superconductivity. However, despite decades of intense effort, there are still large gaps in our understanding of the mechanisms underpinning the formation and competition between such states. New experimental observations of correlated states can provide litmus tests for competing theoretical models. CDWs are a periodic spatial oscillation of charge density, accompanied by a lattice distortion, that occur in crystalline materials due to electron-electron and electron-phonon interactions.[1–3] Despite intense investigation, the physics of CDW formation remains a topic of vigorous debate,[4,5] and the connection to other exotic electronic ground states, most notably superconductivity, remains controversial.[6]

Transition metal dichalcogenides (TMDs) are two-dimensional (2D) layered materials that are tailorable by varying the elemental composition, coordination, symmetry, layer number and separation, and doping.[7,8] TMDs thus provide excellent opportunities to investigate fundamental condensed matter physics in reduced dimensions. CDWs have been discovered in the semimetallic column 4 (d^0) TMDs, $TiSe_2$,[9] and $TiTe_2$,[10] and in the metallic column 5 (d^1) TMDs VS_2,[11] VSe_2,[12] $NbSe_2$,[4,13] TaS_2,[14] and $TaSe_2$.[15] CDWs have not been previously observed in column 6 (d^2) TMDs, which are typically band semiconductors. However, density functional theory calculations have indicted the possibility of CDW formation in heavily-doped bulk[16,17] and monolayer MoS_2,[18,19] and a recent study reported anomalies

in the temperature dependence of the sheet resistance in electron-doped MoS_2, suggesting the possibility of a CDW phase transition.[20] There are two popular mechanisms for CDW formation in TMDs: Fermi surface nesting (FSN; the favoured model in VSe_2, TaS_2, and $TaSe_2$[3,12]), which requires coupling of the Fermi surface and leads to the opening of a small energy gap centred at the Fermi energy; and momentum-dependent electron-phonon coupling (EPC; favoured in $NbSe_2$ and VS_2[11]), which can occur in the absence of strong connections within the Fermi surface. In many cases, not all aspects of the data are adequately described by either model.

MoS_2 is a band semiconductor, column 6 (d^2) TMD with a trigonal prismatic (2H) ground state (Fig. 1c).[7] The band edges derive from $4d$ orbitals,[7] and the bulk material has a 1.29 eV indirect band gap[21] (Fig. 1a). In reciprocal space, the valence band maximum is at the zone centre (Γ), while the conduction band minimum is located midway along Γ–K, producing a sixfold degenerate conduction band with electron pockets at the points labelled Q in Figs. 1a,b. With electron doping, MoS_2 undergoes a metal-insulator transition at a free carrier density of $n_{2D} = 6.7 \times 10^{12}$ cm^{-2}, and exhibits a sharp onset of superconductivity at 6.8×10^{13} cm^{-2}.[22]

Here, we present the discovery of a CDW ground state in bulk potassium-intercalated (and therefore electron-doped) MoS_2 with a simultaneous exhibition of FSN and EPC derived modulations. We demonstrate a metal-insulator transition at 85 K, $(2\sqrt{3} \times 2\sqrt{3})$R30° and 2×2 CDW modulations via atomic-resolution scanning tunnelling microscopy (STM), and a 25 meV energy gap at the Fermi level via tunnelling spectroscopy. The $2\sqrt{3}$ modulation is perfectly matched by a nesting vector connecting the conduction band pockets, while the 2×2 modulation matches a theoretically predicted phonon-mode softening at the M point.[18] We discuss that the two modulations are simple linear combinations of one another, suggesting that the driving mechanisms may be coupled via band folding.

Potassium ions were intercalated into the Van der Waals gaps of a bulk MoS_2 sample using the well-established low-temperature liquid ammonia method.[23] Briefly, high-quality MoS_2

crystals (Manchester Nanomaterials) were degased (523 K, $< 10^{-6}$ mbar) then combined with potassium dissolved in liquid ammonia at 218 K. Potassium intercalation (Fig. 1d) completed after ~ 24 h. X-ray diffraction (XRD) was measured in a reflection geometry (Philips X'Pert) on cleaved samples in an airtight beryllium dome. Magnetic susceptibility measurements (Quantum Design MPMS-7) were performed on samples held in a plastic capsule and sample straw. Four-terminal contacts were attached to the sample using Epotek H21D silver epoxy and transport measurements (Keithley 2400 SMU and Stanford Research Systems SR830) were made on a cold finger below 10^{-5} mbar with a 1 mA current and 10 Kh^{-1} heating rate. STM measurements (Omicron LT-STM) were performed on samples cleaved under ultrahigh vacuum ($< 5 \times 10^{-10}$ mbar) at room temperature to produce an atomically-clean surface of a bulk intercalated sample, and then cooled to 5.5 K for STM measurement.

XRD confirms the crystalline quality of our samples (Fig. 1e); the 00l out-of-plane peaks are shifted with respect to their unintercalated positions, demonstrating the expected 2.2 ± 0.1 Å increase in the layer separation.[23] Magnetic susceptibility and four-terminal resistivity measurements (Figs. 1f and 1g) confirm the onset of superconductivity at $T_\mathrm{c} = 7.0 \pm 0.5$ K.[23,24] The room temperature resistivity ($R_\mathrm{s} \sim 1 \times 10^{-4}$ Ωcm) decreases linearly with temperature (Fig. 1g, red trace), as expected.[25] At 85 K we find a pronounced step increase of $\sim 5 \times 10^{-5}$ Ωcm, marking the location of a metal-insulator transition. Also at 85 K we find an abrupt decrease (-0.02 emu/g) in magnetic susceptibility (Fig. 1h). These features are characteristic of the opening of an energy gap at the Fermi level, and similar behaviour has been attributed to CDW transitions in VS$_2$[11] and TaS$_2$.[26]

Figure 2a displays a topographic STM image of a region free from step edges or adatoms, and that is characteristic of images acquired using different samples and tips. The Fourier transform of this image (Fig. 2b) exhibits hexagonal spots corresponding to a lattice constant, $a = 3.14 \pm 0.07$ Å, in agreement with the calculated lattice constant, 3.176 Å,[28] confirming that we are imaging the surface sulfur atoms of the cleaved sample. A 0.2 monolayer surface
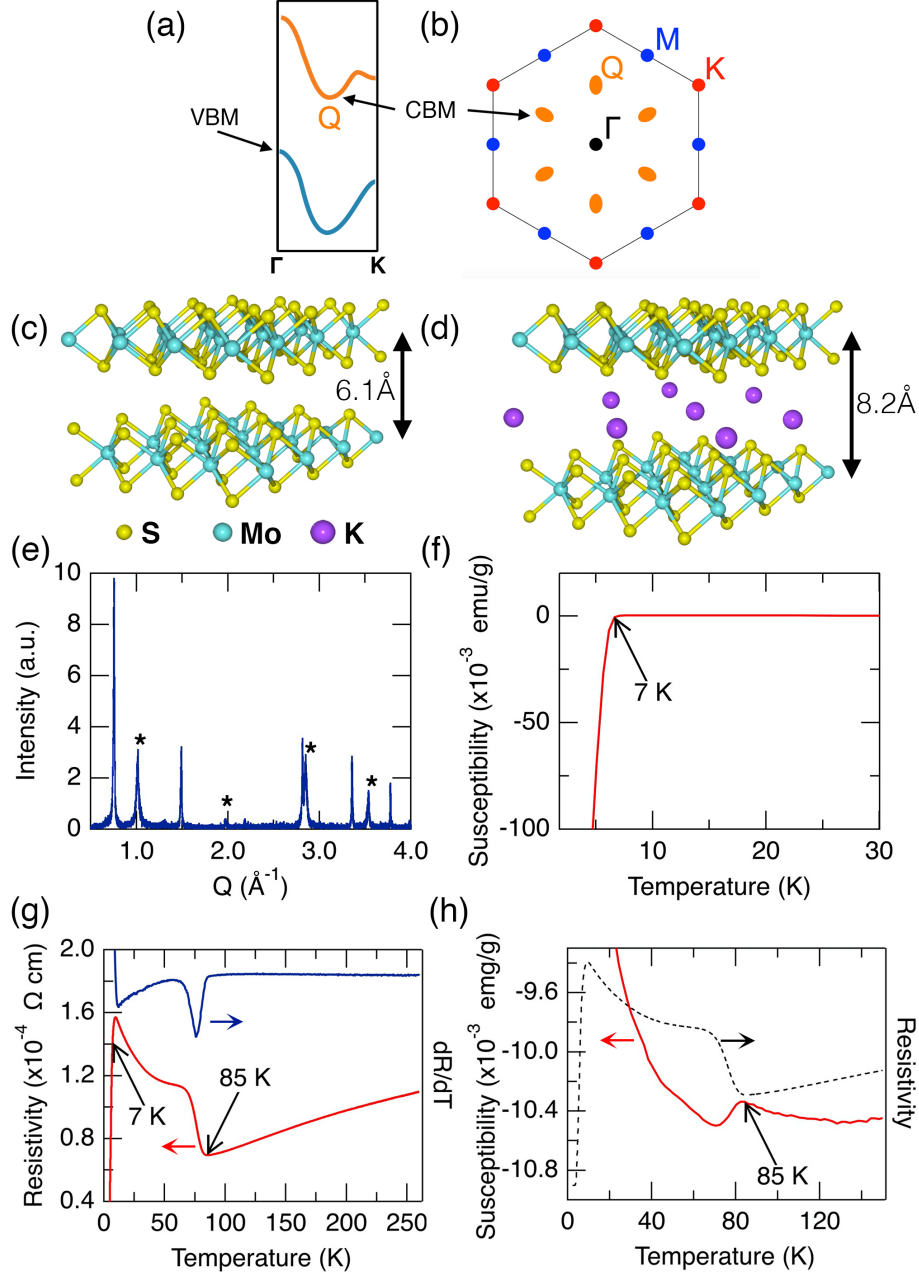
Figure 1: (a) MoS$_2$ band structure schematic highlighting valence/conduction band maximum/minimum (VBM/CBM) (adapted from Ref.[27]). (b) Brillouin zone with high-symmmetry points Γ, K, M, and low-symmetry point Q. (c) Crystal structure of MoS$_2$ and (d) of K$_{0.4}$MoS$_2$. (e) K$_{0.4}$MoS$_2$ x-ray diffraction; asterisks denote unintercalated MoS$_2$ peaks. (f) Magnetic susceptibility (10 Oersted). (g) Resistivity (red trace) showing metal-insulator (85 K) and superconducting transitions (7 K); dR_S/dT is shown on the right axis (blue trace). (h) Magnetic susceptibility (red trace) with a large applied field (10^4 Oe) with resistivity data overlayed (dashed curve; right axis).

5

coverage of potassium ions might be expected if half of the potassium ions in the cleaved layer remain on the surface after cleaving. However, we do not observe any surface potassium ions in our images and attribute this to the surface potassium ions diffusing to step edges or elsewhere while the sample is at room temperature before it is loaded into the STM and cooled. Several defects in Fig. 2a appear as protrusions several nanometres in diameter superimposed on the surface atomic lattice. Similar defects, attributed to molybdenum vacancies or antisites, have been shown to locally enhance the MoS_2 interlayer coupling[29,30]

Figure 2c shows a higher resolution image acquired with a lower imaging bias magnitude $(-100 \, \text{mV})$. This image, and the corresponding Fourier transform (Fig. 2d), reveals a longer-ranged periodicity of 5.8 ± 0.2 Å; i.e., 2 ± 0.2 times the 1×1 lattice, which we interpret as a 2×2 CDW modulation. We notice that the apparent intensity of the 2×2 modulation varies within the image (Fig. 2c), suggesting a nearly-commensurate CDW phase, as observed in STM images of $NbSe_2$,[13] and copper-intercalated $TiSe_2$.[31] Examining again the Fourier transform of the larger area image in Fig. 2b, we see the 2×2 spots are also faintly visible in this data. Indeed, in all images of the $K_{0.4}MoS_2$ surface acquired with sufficient resolution we find evidence for a 2×2 periodicity to a greater or lesser extent depending on the imaging parameters and location on the surface, suggesting that in $K_{0.4}MoS_2$ we have a nearly-commensurate 2×2 CDW state present everywhere throughout the sample surface.

The image in Fig. 2e shows an area where two defects are present. Here, we find an additional periodicity, distinct from both the 1×1 lattice, and the 2×2 modulations. The Fourier transform (Fig. 2f) demonstrates that this periodicity is characterised by a 10.4 ± 0.2 Å real space vector, which is rotated $30°$ with respect to the 1×1 lattice. We note that within uncertainties, this periodicity is $2\sqrt{3}$ times the 1×1 unit cell vector $(= 10.7 \pm 0.4)$, and we therefore label this as a $(2\sqrt{3} \times 2\sqrt{3})R30°$ modulation of the $K_{0.4}MoS_2$ surface. Unlike the 2×2 modulation, the $2\sqrt{3}$ modulation is strongly enhanced within the vicinity of the defect sites. We found such $2\sqrt{3}$ modulations always occur at such defects sites; e.g., the $2\sqrt{3}$ spots are visible in Fig 2b due to the defects in the corresponding STM image, and

further examples are shown in Figs. 2g,h and Supplementary Figure S1). Modulations of the local density of states in the vicinity of defects can occur due to quasiparticle interference (QPI);[32] however, we rule out QPI in the present case since the modulation is dispersionless[32] (see the spatially-resolved tunnelling spectroscopy presented below). It is possible also to draw comparison to $NbSe_2$, where the 3×3 CDW modulation was found to persist above T_{CDW} in patches surrounding defects.[13] However, our measurements of defects in $K_{0.4}MoS_2$ at 5.5, 10, and 77 K show negligible change in the spatial extent of the $2\sqrt{3}$ modulation surrounding the defects with temperature (see Supplementary Figure S1). Moreover, we also observe phase slip boundaries in the $2\sqrt{3}$ modulation for closely spaced defects, similar to observations of phase boundaries in CDW modulations seen in $NbSe_2$[33] and $TiSe_2$.[34] We show an example of this in Fig. 2g, which shows a filled-state STM image where two defects are present (the corresponding Fourier transform is shown in Fig. 2h). The two defects exhibit $2\sqrt{3}$ modulations, but these two modulations are not in phase, leading to a phase slip boundary between them, which we highlight with a white arrow in Fig. 2g. Further analysis and discussion of this phase slip boundary can be found in Supplementary Figure S2. The implication of these observations is that the $2\sqrt{3}$ modulation can be attributed to a CDW whose enhancement at defect sites is an intrinsic property, and not due to QPI or an incompletely formed CDW phase.

Other non-CDW explanations for the observed 2×2 and $2\sqrt{3}$ periodicities can be ruled out. The precise arrangement of the potassium ions in $K_{0.4}MoS_2$ is not known;[23,28] however, the $K_{0.4}MoS_2$ stoichiometry[23] and hexagonal symmetry of the crystal suggests a hexagonal arrangement of the average positions of the potassium ions, with a lattice constant of $\sqrt{5/2}a$. Thus, even allowing for all possible rotational orientations of the potassium ion layer with respect to the top MoS_2 layer, we can rule out both a direct influence of the potassium ion positions, and Moiré interference between the MoS_2 and potassium ion layers as explanations for either periodicity. Moiré effects due to strain at defect sites can be additionally ruled out by the observation that the characteristic length of the modulation does not vary with

distance from the defect centre as would be expected for a point-source lattice distortion derived Moiré interference.

Figure 3 presents scanning tunnelling spectroscopy (STS) measurements of $K_{0.4}MoS_2$. Point spectra show a bulk band gap of around 1.2 eV (Fig. 3a), consistent with previous measurements,[30] and calculations.[28] Higher-resolution measurements at the conduction band edge (Fig. 3b) show the band minimum is located ~ 25 meV below the Fermi level, in agreement with ARPES measurements of potassium-doped MoS_2,[35] and a similar band shift in copper intercalated $TiSe_2$.[31]

We also find an energy gap at the Fermi level (Figs. 3b,3c); we measure the the gap as the point where a quadratic fit to the gap intersects the conduction band, and take the gap to be twice this value, yielding $2\Delta = 24 \pm 4$ meV. There was no measurable difference between spectra taken on or away-from defect sites, demonstrating that the gap occurs across the entire surface.

We have measured spatially-resolved conductivity, $g(r, V)$, where r is the tip position and V the sample bias (see Supplementary Figure S3); when integrated over r (Fig. 3c) this yields good agreement with the point spectroscopy in Fig. 3b. We deconvolve contributions associated with the different superlattice modulations by taking a 2D Fourier transform of $g(r, V)$ for each value of bias, to obtain conductivity as a function of the reciprocal space vector q. We identify in this data the expected 1×1, 2×2, and $2\sqrt{3}$ reciprocal lattice vectors, and show the intensity variation of these spots as a function of bias in Fig. 3d. The observation that these spots occur at the same values of q for each value of bias (See Supplementary Figure S3) rules out QPI origins for these modulations, and we do not observe any additional spots for any values of the applied bias. The 1×1 spot intensity variation (Fig. 3d) closely matches the spatially-averaged conductance (Fig. 3c). In contrast, the $2\sqrt{3}$ spots exhibit a gap feature and peaked intensities either side of the Fermi level. The intensity variation of the 2×2 spots follow similarly to the $2\sqrt{3}$ spots, although the signal-to-noise ratio is insufficient to say conclusively whether or not the gap exists in the 2×2 data.

Concentrating on the $2\sqrt{3}$ curve, which has the better signal-to-noise ratio, we measure peak maxima at $\pm 3.1 \pm 0.1$ mV, i.e., separated about the Fermi level by a width of 6.2 ± 0.2 mV. Alternatively, if we measure the width from the outer edges of the peaks, we find a width of 26 ± 2 mV. These widths compare well to the gap width estimation from our point spectra in Fig. 3b. Thus, the spatially-resolved tunnelling spectroscopy data shown in Fig. 3, and the fact that the Fermi level gap in STS spectra occurs far from defect sites where the 2×2 modulation persists but the $2\sqrt{3}$ modulation doesn't, suggests that the energy gap at the Fermi level correlates to both the 2×2 and $2\sqrt{3}$ spatial modulations observed in our STM and STS images.

Our observations of a metal-insulator transition at 85 K and a 24 ± 4 meV energy gap centred at the Fermi level are suggestive of a FSN-driven CDW in $K_{0.4}MoS_2$. The necessary FSN vectors exist in the $K_{0.4}MoS_2$ electronic structure due to the fact that potassium intercalation of MoS_2 creates electron pockets at the Q points. The length of the vector, $\mathbf{q}$ (Fig. 4a), that connects the Fermi surfaces at Q is $|\mathbf{\Gamma K}|/2$, i.e., $|\mathbf{q}| = \frac{|\mathbf{b}|}{4}/\cos\frac{\pi}{6} = b/2\sqrt{3}$, where $\mathbf{b}$ is the reciprocal lattice vector. There are three pairs of such nesting vectors, each rotated $30°$ to the 1×1 surface sulfur lattice. Thus, the vectors $\mathbf{q}$ connecting neighbouring Q points provide an excellent match to our observed $(2\sqrt{3} \times 2\sqrt{3})R30°$ modulation in STM and STS data. This provides strong evidence for a FSN-driven $2\sqrt{3}$ CDW phase in $K_{0.4}MoS_2$ that is localised at, or enhanced by defects in the MoS_2 sheets. The reason for this enhancement at defects is that the defects locally enhance the interlayer coupling,[29,30] resulting in a lowering of the band edge at the Q point and thus an increased occupancy of the bulk-like electron pockets[7] and a corresponding enhancement of the $2\sqrt{3}$ FSN.

However, FSN cannot explain the appearance of the 2×2 periodicity in our STM data, because the electronic bands at the M-point are much higher in energy than the band minima.[7] However, calculations of the MoS_2 phonon band structure as a function of electron doping have demonstrated phonon softening at the M point, becoming imaginary for electron doping levels exceeding ~ 0.14 electrons per molybdenum atom.[18,36] The M point lies on the

Brillouin zone boundary along the reciprocal lattice vector direction (Fig. 4a), and as such is inherently associated with a 2×2 periodicity. This strongly suggests that momentum-dependent EPC can account for the formation of the 2×2 phase in $K_{0.4}MoS_2$.

Thus, our observations of a metal-insulator transition at 85 K, the opening of a ~ 25 meV energy gap at the Fermi level, and the real space observation of a $2\sqrt{3}$ modulation in STM and STS data provide compelling evidence for the existence of a FSN-driven CDW phase, where the nesting vector connects electron pockets at the Q points. This $2\sqrt{3}$ phase is locally enhanced by defects in the MoS_2 sheets that locally alter the interlayer coupling and enhances the electron pockets at the Q points. Simultaneously, we observe a nearly-commensurate 2×2 modulation that matches a predicted 2×2 EPC-driven CDW due to phonon softening at the M point. As has been a feature of several previous reports of CDW phases in TMDs,[3,4] it is not possible to fully describe all of our data with *either* a FSN *or* EPC model independently.

We suggest that the coexistence of the 2×2 and $2\sqrt{3}$ phases is possible in part due to the effect of band folding. We illustrate the reciprocal space vectors of the $2\sqrt{3}$ periodicity (u_1 and u_2) and 2×2 periodicity (v_1 and v_2) in Fig. 4b, and it can be seen that these are simple linear combinations of one another (e.g., $v_1 = u_1 + u_2$). Thus, band folding established by the shorter periodicity (illustrated by the hexagonal tiling in Fig. 4b) will result in the band minimum at Q and the soft phonon mode at M being mapped back onto the zone center, providing an opportunity for the two mechanisms to couple. The fact that the two modulations are simple linear combinations of one another also provides an explanation for why the Fermi level gap we measure in STS spectra contains 2×2 as well as $2\sqrt{3}$ periodicity.

We have presented the discovery of a CDW ground state in $K_{0.4}MoS_2$, which is also the first observation of a CDW phase in a d^2 (column 6) TMD. Owing to the unique band structure of $K_{0.4}MoS_2$ compared to d^0 and d^1 TMDs, our results provide new insight into the formation mechanisms of CDWs. We observe a metal-insulator transition at 85 K, a ~ 25 meV energy gap centred at the Fermi level, and 2×2 and $2\sqrt{3}$ periodicities that can

be explained, respectively, by EPC and FSN mechanisms. The $2\sqrt{3}$ periodicity is observed exclusively near defects, suggesting that the coexistence of FSN and EPC phases can be attributed to their delicate sensitivity to the band edge and the strength of the interlayer electronic coupling. Moreover, our observations suggest that CDW phases might be discoverable in other column 6 TMDs such as $MoSe_2$, WS_2, and WSe_2[37] at high electron-doping, and whose investigation might provide further insight into the physics of CDW formation.

Acknowledgement

Supporting Information Available

The Supporting Information is available free of charge on the ACS Publications website at DOI: XXXX. STM images of $2\sqrt{3}$ modulations at defect sites acquired at 5.5, 10, and 77 K. STM images and analysis of phase slip boundaries. Spatially-resolved tunnelling spectroscopy of $2\sqrt{3}$ modulation. The data created during this research are openly available via zenodo.org at https://doi.org/10.5281/zenodo.3696856.

References

(1) Grüner, G. *Density Waves in Solids*; Perseus Publishing: Cambridge, Massachusetts, 1994; pp 1–85.

(2) Zhu, X.; Cao, Y.; Zhang, J.; Plummer, E. W.; Guo, J. Classification of charge density waves based on their nature. *Proc. Natl. Acad. Sci.* **2015**, *112*, 2367–2371.

(3) Rossnagel, K. On the origin of charge-density waves in select layered transition-metal dichalcogenides. *J. Phys. Condens. Matter* **2011**, *23*, 213001.

(4) Ugeda, M. M. et al. Characterization of collective ground states in single-layer $NbSe_2$. *Nat. Phys.* **2016**, *12*, 92–97.

(5) Zhu, X.; Guo, J.; Zhang, J.; Plummer, E. W. Misconceptions associated with the origin of charge density waves. *Adv. Phys. X* **2017**, *2*, 622–640.

(6) Gabovich, A. M.; Voitenko, A. I.; Ausloos, M. Charge- and spin-density waves in existing superconductors: Competition between Cooper pairing and Peierls or excitonic instabilities. *Phys. Rep.* **2002**, *367*, 583–709.

(7) Chhowalla, M.; Shin, H.; Eda, G.; Li, L. The chemistry of two-dimensional layered transition metal dichalcogenide nanosheets. *Nat. Chem.* **2013**, *5*, 263.

(8) Manzeli, S.; Ovchinnikov, D.; Pasquier, D.; Yazyev, O. V.; Kis, A. 2D transition metal dichalcogenides. *Nat. Rev. Mater.* **2017**, *2*, 17033.

(9) Sugawara, K.; Nakata, Y.; Shimizu, R.; Han, P.; Sato, T.; Hitosugi, T.; Sato, T.; Takahashi, T. Unconventional Charge-Density-Wave Transition in Monolayer 1T-$TiSe_2$. *ACS Nano* **2015**, *10*, 1341–1345.

(10) Chen, P.; Pai, W. W.; Chan, Y. H.; Takayama, A.; Xu, C. Z.; Karn, A.; Hasegawa, S.; Chou, M. Y.; Mo, S. K.; Fedorov, A. V.; Chiang, T. C. Emergence of charge density waves and a pseudogap in single-layer $TiTe_2$. *Nat. Commun.* **2017**, *8*, 516.

(11) Mulazzi, M.; Chainani, A.; Katayama, N.; Eguchi, R.; Matsunami, M.; Ohashi, H.; Senba, Y.; Nohara, M.; Uchida, M.; Takagi, H.; Shin, S. Absence of nesting in the charge-density-wave system 1T-VS_2 as seen by photoelectron spectroscopy. *Phys. Rev. B* **2010**, *82*, 075130.

(12) Strocov, V. N.; Shi, M.; Kobayashi, M.; Monney, C.; Wang, X.; Krempasky, J.; Schmitt, T.; Patthey, L.; Berger, H.; Blaha, P. Three-dimensional electron realm in VSe_2 by soft-x-ray photoelectron spectroscopy: Origin of charge-density waves. *Phys. Rev. Lett.* **2012**, *109*, 086401.

(13) Arguello, C. J.; Chockalingam, S. P.; Rosenthal, E. P.; Zhao, L.; Gutiérrez, C.; Kang, J. H.; Chung, W. C.; Fernandes, R. M.; Jia, S.; Millis, A. J.; Cava, R. J.; Pasupathy, A. N. Visualizing the charge density wave transition in 2H-NbSe2 in real space. *Phys. Rev. B* **2014**, *89*, 235115.

(14) Wilson, J. A.; Di Salvo, F. J.; Mahajan, S. Charge-density waves and superlattices in the metallic layered transition metal dichalcogenides. *Adv. Phys.* **2001**, *50*, 1171–1248.

(15) Liu, R.; Tonjes, W. C.; Greanya, V. A.; Olson, C. G.; Frindt, R. F. Fermi surface of and its relation to the charge-density wave. *Phys. Rev. B* **2000**, *61*, 5212–5216.

(16) Enyashin, A. N.; Seifert, G. Density-functional study of Li_xMoS_2 intercalates ($0 \leq x \leq 1$). *Comput. Theor. Chem.* **2012**, *999*, 13–20.

(17) Chen, X. B.; Chen, Z. L.; Li, J. Critical electronic structures controlling phase transitions induced by lithium ion intercalation in molybdenum disulphide. *Chinese Sci. Bull.* **2013**, *58*, 1632–1641.

(18) Rösner, M.; Haas, S.; Wehling, T. O. Phase diagram of electron-doped dichalcogenides. *Phys. Rev. B* **2014**, *90*, 245105.

(19) Zhuang, H. L.; Johannes, M. D.; Singh, A. K.; Hennig, R. G. Doping-controlled phase transitions in single-layer MoS_2. *Phys. Rev. B* **2017**, *96*, 165305.

(20) Piatti, E.; Chen, Q.; Tortello, M.; Ye, J.; Gonnelli, R. S. Possible charge-density-wave signatures in the anomalous resistivity of Li-intercalated multilayer MoS 2. *Appl. Surf. Sci.* **2018**, *461*, 269–275.

(21) Mak, K. F.; Lee, C.; Hone, J.; Shan, J.; Heinz, T. F. Atomically thin MoS2: A new direct-gap semiconductor. *Phys. Rev. Lett.* **2010**, *105*, 136805.

(22) Ye, J. T.; Zhang, Y. J.; Akashi, R.; Bahramy, M. S.; Arita, R.; Iwasa, Y. Superconducting dome in a gate-tuned band insulator. *Science* **2012**, *338*, 1193–1196.

(23) Zhang, R.; Tsai, I. L.; Chapman, J.; Khestanova, E.; Waters, J.; Grigorieva, I. V. Superconductivity in Potassium-Doped Metallic Polymorphs of MoS$_2$. *Nano Lett.* **2016**, *16*, 629–636.

(24) Woollam, J. A.; Somoano, R. B. Superconducting critical fields of alkali and alkaline-earth intercalates of MoS$_2$. *Phys. Rev. B* **1976**, *13*, 3843–3853.

(25) Lu, J. M.; Zheliuk, O.; Leermakers, I.; Yuan, N. F.; Zeitler, U.; Law, K. T.; Ye, J. T. Evidence for two-dimensional Ising superconductivity in gated MoS$_2$. *Science* **2015**, *350*, 1353–1357.

(26) Kratochvilova, M.; Hillier, A. D.; Wildes, A. R.; Wang, L.; Cheong, S. W.; Park, J. G. The low-temperature highly correlated quantum phase in the charge-density-wave 1T-TaS2 compound. *npj Quantum Mater.* **2017**, *2*, 42.

(27) Splendiani, A.; Sun, L.; Zhang, Y.; Li, T.; Kim, J.; Chim, C. Y.; Galli, G.; Wang, F. Emerging photoluminescence in monolayer MoS$_2$. *Nano Lett.* **2010**, *10*, 1271–1275.

(28) Andersen, A.; Kathmann, S. M.; Lilga, M. a.; Albrecht, K. O.; Hallen, R. T.; Mei, D. First-principles characterization of potassium intercalation in hexagonal 2H-MoS$_2$. *J. Phys. Chem. C* **2012**, *116*, 1826–1832.

(29) Sengoku, N.; Ogawa, K. Investigations of electronic structures of defects introduced by ar ion bombardments on MoS$_2$ by scanning tunneling microscopy. *Jpn. J. Appl. Phys.* **1995**, *34*, 3363–3367.

(30) Bampoulis, P.; Van Bremen, R.; Yao, Q.; Poelsema, B.; Zandvliet, H. J.; Sotthewes, K. Defect Dominated Charge Transport and Fermi Level Pinning in MoS2/Metal Contacts. *ACS Appl. Mater. Interfaces* **2017**, *9*, 19278–19286.

(31) Yan, S.; Iaia, D.; Morosan, E.; Fradkin, E.; Abbamonte, P.; Madhavan, V. Influence of Domain Walls in the Incommensurate Charge Density Wave State of Cu Intercalated 1T-TiSe2. *Phys. Rev. Lett.* **2017**, *118*, 106405.

(32) Chen, L.; Cheng, P.; Wu, K. Quasiparticle interference in unconventional 2D systems. *J. Phys. Condens. Matter* **2017**, *29*, 103001.

(33) Soumyanarayanan, A.; Yee, M. M.; He, Y.; van Wezel, J.; Rahn, D. J.; Rossnagel, K.; Hudson, E. W.; Norman, M. R.; Hoffman, J. E. Quantum phase transition from triangular to stripe charge order in $NbSe_2$. *Proc. Natl. Acad. Sci.* **2013**, *110*, 1623–1627.

(34) Novello, A. M.; Spera, M.; Scarfato, A.; Ubaldini, A.; Giannini, E.; Bowler, D. R.; Renner, C. Stripe and Short Range Order in the Charge Density Wave of $1T-Cu_xTiSe_2$. *Phys. Rev. Lett.* **2017**, *118*, 017002.

(35) Eknapakul, T.; King, P. D. C.; Asakawa, M.; Buaphet, P.; He, R. H.; Mo, S. K.; Takagi, H.; Shen, K. M.; Baumberger, F.; Sasagawa, T.; Jungthawan, S.; Meevasana, W. Electronic structure of a quasi-freestanding MoS2 monolayer. *Nano Lett.* **2014**, *14*, 1312–1316.

(36) Garcia-Goiricelaya, P.; Lafuente-Bartolome, J.; Gurtubay, I. G.; Eiguren, A. Emergence of large nonadiabatic effects induced by the electron-phonon interaction on the complex vibrational quasiparticle spectrum of doped monolayer MoS_2. *Phys. Rev. B* **2020**, *101*, 54304.

(37) Gusakova, J.; Wang, X.; Shiau, L. L.; Krivosheeva, A.; Shaposhnikov, V.; Borisenko, V.; Gusakov, V.; Tay, B. K. Electronic Properties of Bulk and Monolayer TMDs: Theoret-

ical Study Within DFT Framework (GVJ-2e Method). *Phys. Status Solidi* **2017**, *214*, 1700218.
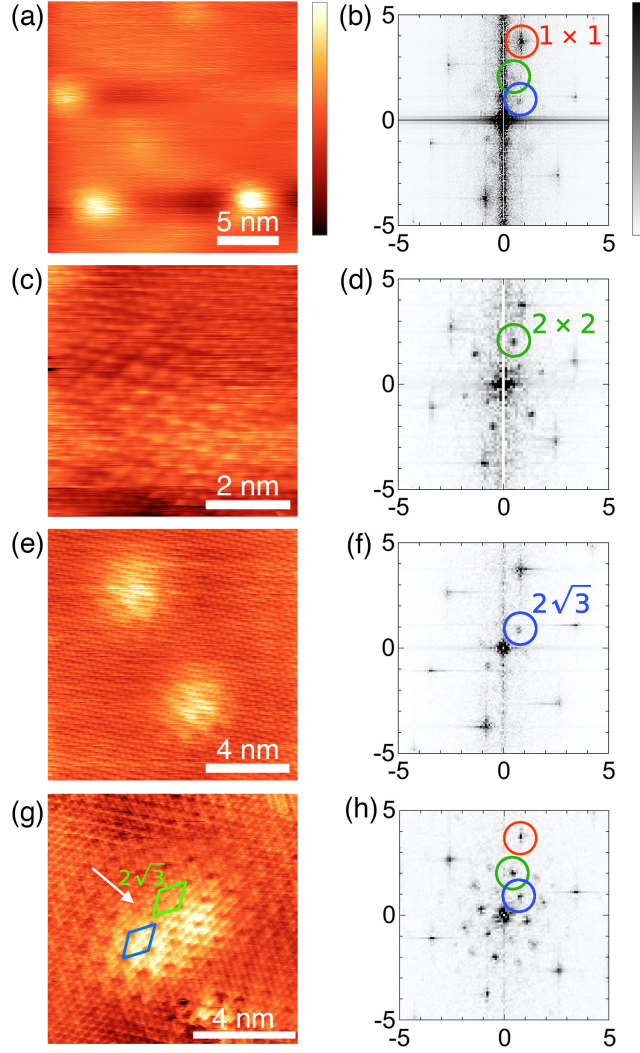
Figure 2: (a,c,e) STM topographic images of $K_{0.4}MoS_2$ (5.5 K), and (b,e,f) their corresponding 2D Fourier transforms. Bragg spots corresponding to the 1×1 surface sulphur lattice are seen in all images, while to a lesser or greater extent 2×2 and $2\sqrt{3}$ periodicities are also observed (see text). Image parameters: (a) -150 mV, 20 pA, z-range 1.5 nm; (c,e) -100 mV, 30 pA, z-range 700 pm. FFT axes are in nm^{-1} units. (g) Filled-state STM image of a pair of closely-spaced defects in $K_{0.4}MoS_2$. 1×1, 2×2, and $2\sqrt{3}$ periodicities can be seen in the image and its Fourier transform in panel (h). A phase slip boundary (white arrow) exists between the two regions of $2\sqrt{3}$ periodicity, which we highlight on panel (g) by adding a blue rhombus to indicate the phase of the $2\sqrt{3}$ modulation at the bottom left defect site, and a green rhombus to indicate the $2\sqrt{3}$ phase of the top right defect.
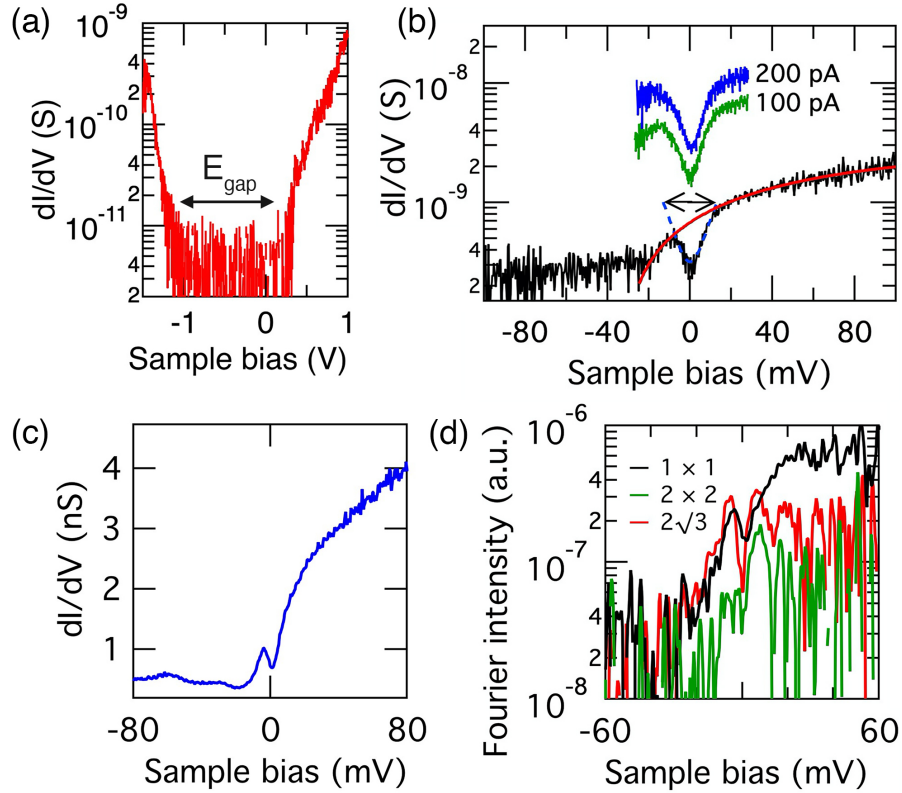
Figure 3: Point tunnelling spectroscopy of $K_{0.4}MoS_2$ highlighting (a) the ~ 1.2 eV band gap, and (b) the conduction band minimum at -25 meV and gap at the Fermi level; curve fits are to the band edge (red) and energy gap (dashed blue). (c) Spatial average of dI/dV. (d) Fourier spot intensities for the 1×1, 2×2, and $2\sqrt{3}$ lattice spots (see Supplementary Figure S3 for corresponding dI/dV images at ± 5 mV). Tunnelling spectra were acquired by measuring current as a function of voltage with the feedback loop off. Set-point parameters: (a) -1.5 V, 50 pA; (b) black: -100 meV, 30 pA; green -30 meV, 100 pA; blue: -30 meV, 200 pA. All data 5.5 k, except panel (b) 10 K.

(a) (1×1)

M (2×2)

Q

q

K

Γ

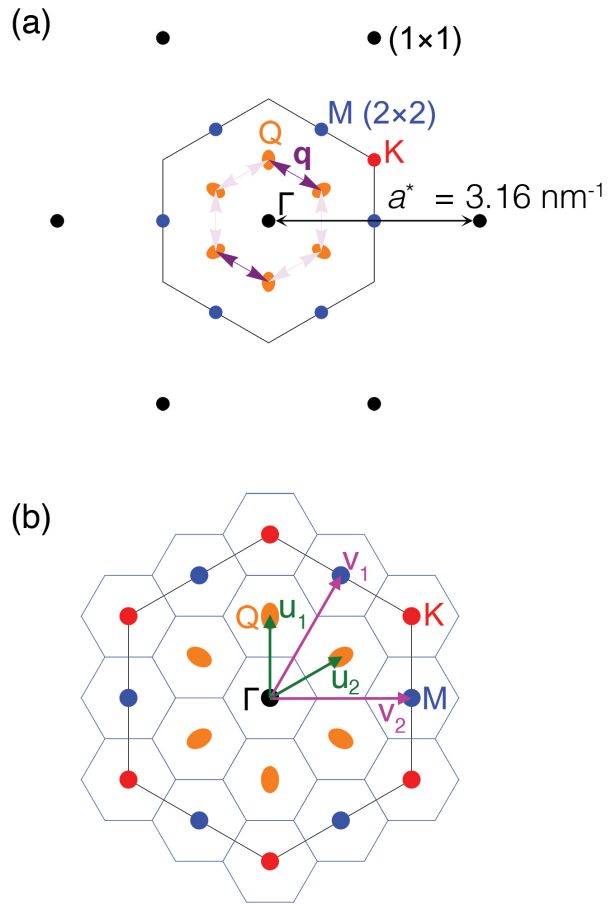a^* = 3.16 nm^{-1}

(b)

v_1

Q u_1

K

u_2

Γ

v_2

M

Figure 4: (a) Reciprocal lattice (black spots) and Brillouin zone with high symmetry points Γ, K, and M. Band minima at the low symmetry points, Q, lying half way along Γ − K, are shown. (b) Brillouin zone drawn with an overlaid $(2\sqrt{3} \times 2\sqrt{3})$R30° unit cell. Vectors u_1, u_2 and v_1, v_2 indicate the Q and M points, respectively.
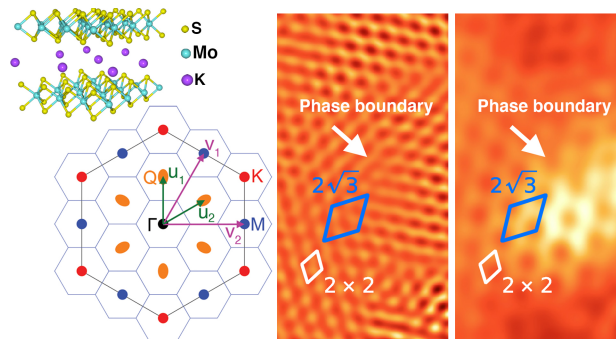

S
Mo
K

v_1
Q u_1
K
u_2
Γ
v_2 M

Phase boundary

Phase boundary

$2\sqrt{3}$

$2\sqrt{3}$

2 × 2

2 × 2

Figure 5: TOC graphic

SUPPLEMENTARY INFORMATION:

Charge density waves in electron-doped molybdenum disulfide

Mohammed K. Bin Subhan,[1] Asif Suleman,[1,2] Gareth Moore,[1,2]

Peter Phu,[2,3] Moritz Hoesch,[4,†] Hidekazu Kurebayashi,[2,3]

Christopher A. Howard,[1] and Steven R. Schofield[1,2]

[1]Department of Physics and Astronomy, University College London, WC1E 6BT, London, UK

[2]London Centre for Nanotechnology, University College London, WC1H 0AH, London, UK

[3]Department of Electronic and Electrical Engineering, University College London, WC1E 6BT, London, UK

[4]Photon Science, Deutsches Elektronen-Synchrotron (DESY), Notkestrasse 85, 22607 Hamburg, Germany

[†]Previously at: Diamond Light Source, Didcot OX11 0DE, UK

June 19, 2021

Supplementary Data

Supplementary Figure S1 shows STM topographic images of three defects on $K_{0.4}MoS_2$ acquired at 77, 10, and 5.5 K, with their corresponding Fourier transform. The 1×1 surface sulfur lattice is clearly observed in each image, as well as the $(2\sqrt{3} \times 2\sqrt{3})R30°$ modulation at the defect site. In each case, the spatial extent of the enhancement due to the defect is about 5 nm, and the $2\sqrt{3}$ modulation extends over the same distance, becoming weaker at distances further from the defect site. This behaviour contrasts to observations of defects in $NbSe_2$ [1], where the spatial extend of the 3×3 modulation varied from several nanometres, to covering the entire surface over a similar temperature range variation. We also note in Supplementary Figures. S1c and S1e that we observe no significant differences in the appearance of the surface above and below the expected superconducting transition temperature ($\sim$ 7 K).
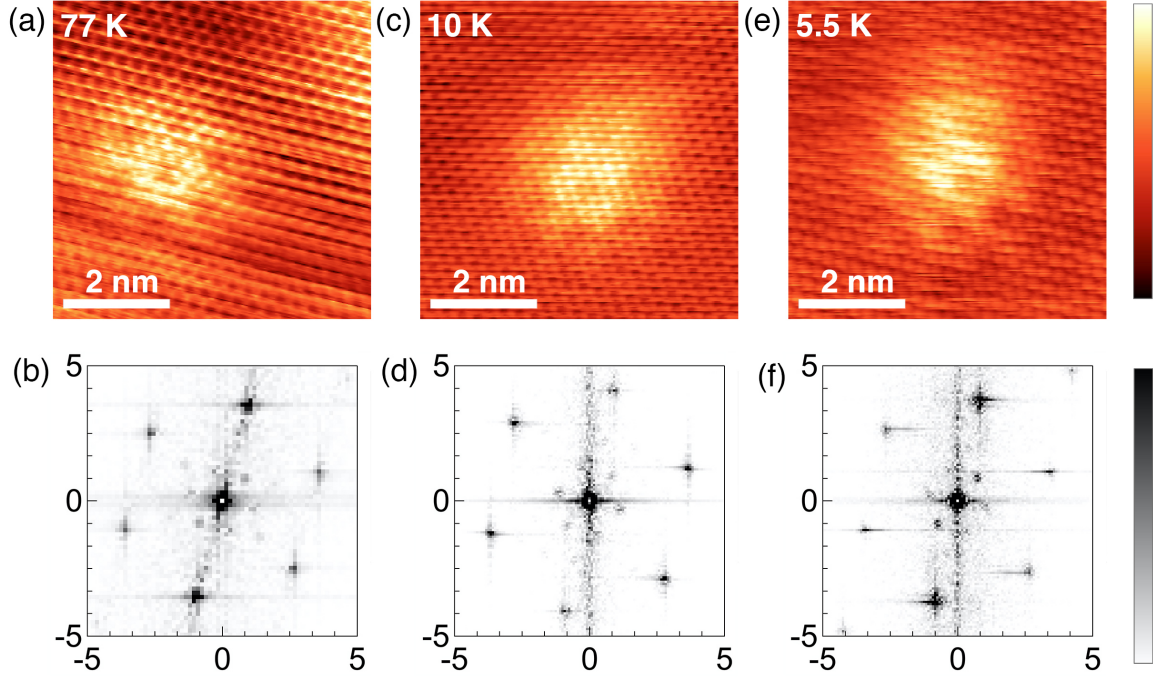
Supplementary Figure S1: STM topographic images of defects in $K_{0.4}MoS_2$ taken at (a) 77 K, (c) 10 K, (e) 5.5 K. The corresponding Fourier transforms are shown in panels (b), (d), and (f). Image parameters: (a) -400 mV, 50 pA, z-range 230 pm; (c) -100 mV, 30 pA, z-range 500 pm; (e) -100 mV, 30 pA, z-range 840 pm;

In the case that two defects occur in close proximity one another, we observe phase slip boundaries in the $2\sqrt{3}$ modulation, similar to the phase slip boundaries observed in the 3×3 CDW in $NbSe_2$ [2]. We illustrate this in Supplementary Figure S2(a), which shows a filled-state STM image of 10×10 nm^2 area where two defects are present. The 2D Fourier transform of this image is shown in Supplementary Figure. S2(b) and highlights that all three periodicities, 1×1, 2×2, and $2\sqrt{3}$, are all present in this image. Each of the two defects has an accompanying $(2\sqrt{3} \times 2\sqrt{3})R30°$ modulation, but the two modulations are not in phase spatially, leading to a phase slip boundary between them, indicated by the white arrow. The phase change can be recognised by observing the hexagonal dark spot patterns in Supplementary Figure S2(a); as a guide to the eye we have drawn a blue rhombus to indicate the phase of the $2\sqrt{3}$ modulation at the bottom left defect site, and a green rhombus to indicate the $2\sqrt{3}$ phase of the top right defect.

In Supplementary Figures S2(c-e) we have use Fourier filtering to further highlight the features of this image. Supplementary Figure S2(d) has been low pass filtered to remove all of the regular periodicities in the image, leaving behind only the aperiodic background generated by the defect envelop function. The two bright protrusions in this image can be attributed to
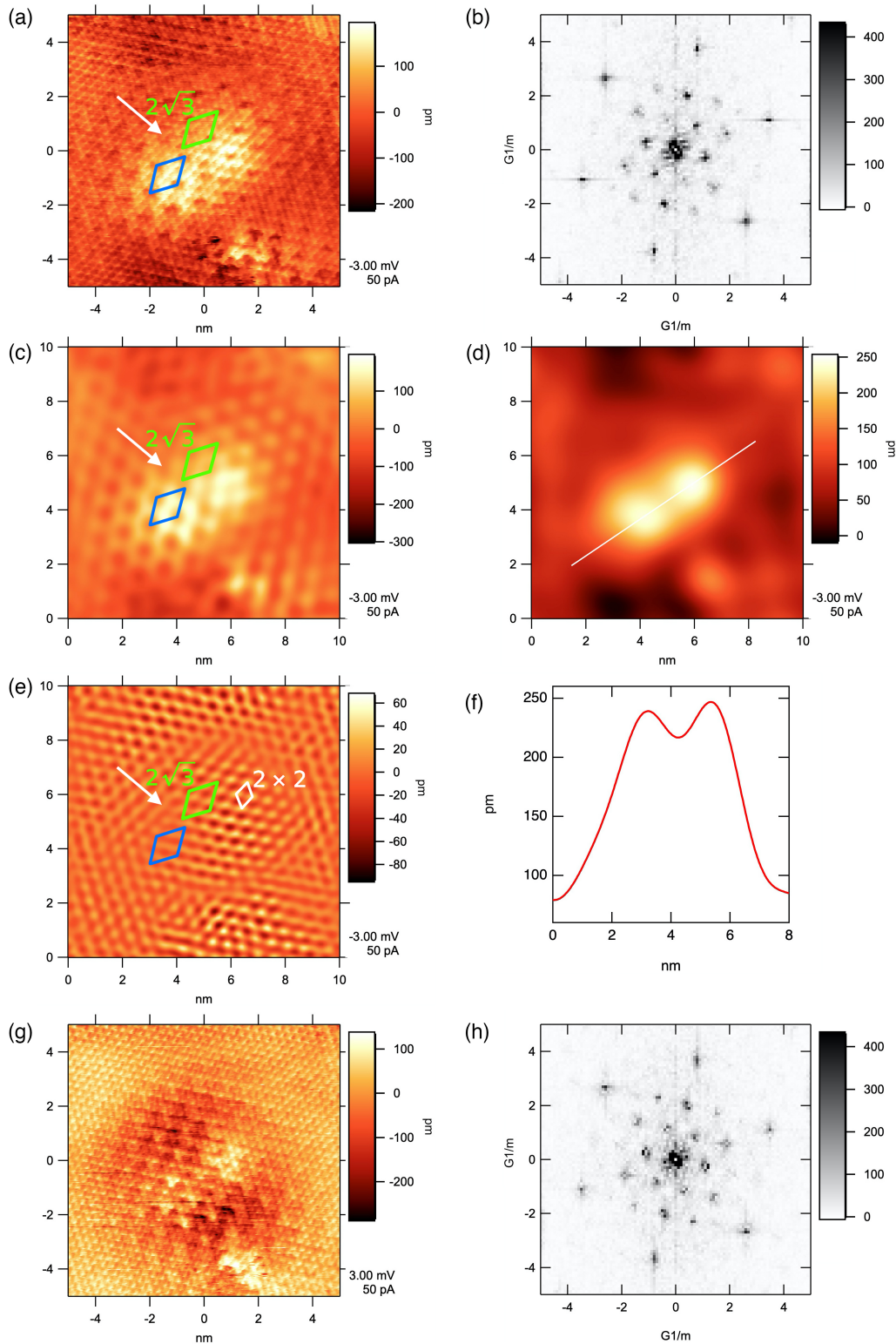
Supplementary Figure S2: (a) Filled-state STM image of a pair of closely-spaced defects in $K_{0.4}MoS_2$, with corresponding 2D Fourier transform shown in panel (b). 1×1, 2×2, and $2\sqrt{3}$ periodicities can be seen in the image and its Fourier transform. The arrow annotation on panel (a) highlights the location of a phase slip boundary in the $2\sqrt{3}$ modulation. (c-e) These three images are the same image from panel (a), that have been Fourier filtered as: (c) low-pass with a cutoff at 1.4 nm^{-1} to remove contributions other than the $2\sqrt{3}$ lattice and the very low frequency aperiodic contributions to the topography. (d) low-pass Fourier filtered with a cutoff at 0.8 nm^{-1}, which also removes the $2\sqrt{3}$ lattice and allows determination of the defect locations. (e) band filtered at six pockets around the 2×2 spots. (f) Line profile from image (d) showing the maxima of the defect envelope functions. (g) Empty-state STM image of the same area as panel (a). (h) Fourier transform of (g).

3
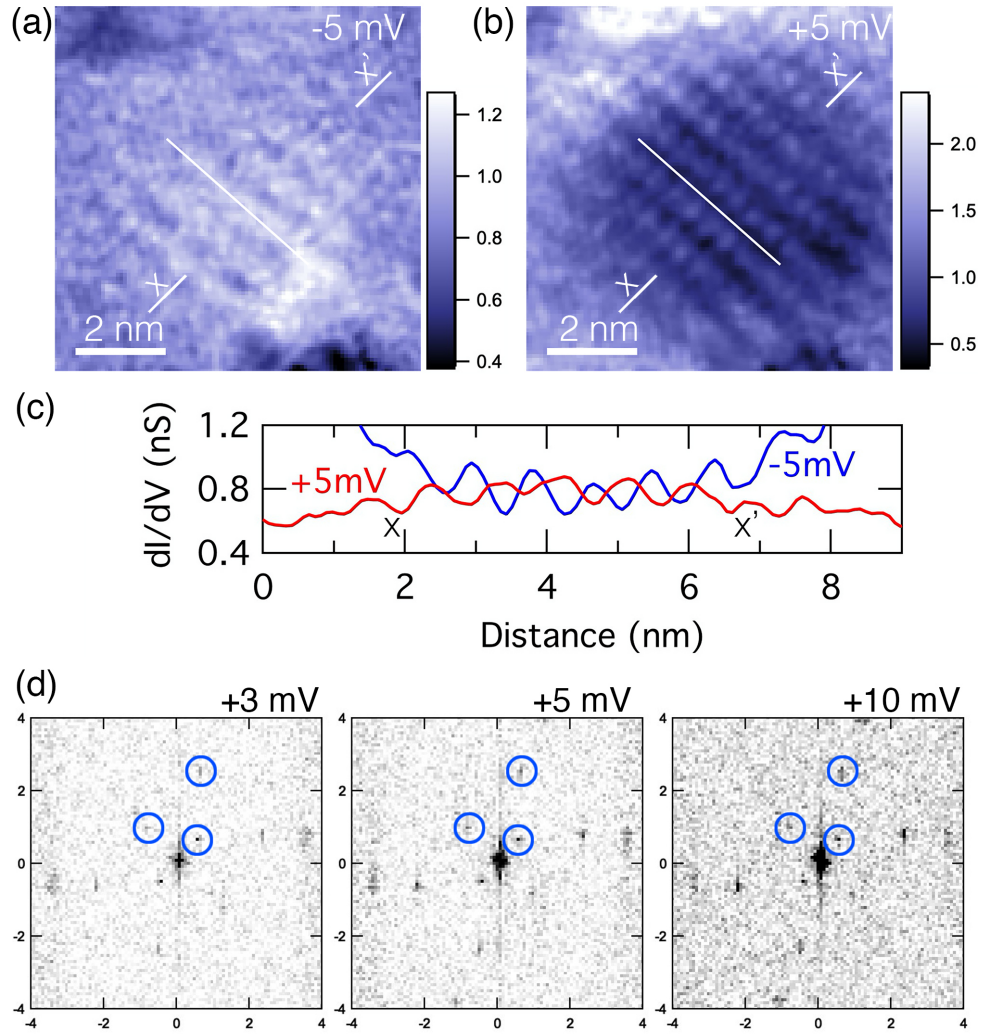
Supplementary Figure S3: (a,b) dI/dV maps (nS) at -5 meV and $+5$ meV, respectively and corresponding Fourier transforms. (c) Line profiles $x - x'$ as indicated in panels a and b. (d) Fourier transforms of the dI/dV maps at 3, 5, and 10 mV, highlighting that the superlattice periodicities are dispersionless.

the two individual defect sites. The line profile in Supplementary Figure S2(f) was taken across the defect to measure their separation, which was determined to be ~ 2.2 nm. Supplementary Figure S2(c) shows the filled state image from Supplementary Figure S2(a) low pass filtered slightly less aggressively such that the $2\sqrt{3}$ modulation still contributes to the filtered image and shows both the $2\sqrt{3}$ modulation and phase slip boundary clearly. We also notice in this image that, as with the other data presented, the intensity of the $2\sqrt{3}$ modulation decreases with distance from the centre of the defect. To illustrate the 2×2 lattice, we also Fourier filter Supplementary Figure S2(a) by the 2×2 spots, and the resulting image is shown in Supplementary Figure S2(e). This image shows that the 2×2 modulation extends over the entire image, with slightly varying intensity across the image, as expected for a nearly-commensurate CDW. It is also notable that no evidence of a phase slip boundary can be seen in the 2×2 modulation. Supplementary Figure S2(g) shows an empty-state image of the same region of the surface, which was acquired simultaneously with Supplementary Figure S2(a), and the corresponding 2D Fourier transform is shown in Supplementary Figure S2(h).

In Supplementary Figures S3(a,b) we show conductivity maps for $V = \pm 5$ mV, over an 8×8 nm^2 region of the surface where a single defect is present. Line profiles across this data (Supplementary Figures S3(c)) highlight both the protrusion/depression nature of the defect envelope [3], and a π phase shift in the $2\sqrt{3}$ modulation. This phase shift in the $2\sqrt{3}$ lattice between the occupied and unoccupied states is similar to previous observations in graphite [4], and is expected within a FSN CDW model. Supplementary Figure S3(d) shows Fourier transforms of the dI/dV maps at 3, 5, and 10 mV, highlighting the absence of dispersion.

References

1. Arguello, C. J. *et al.* Visualizing the charge density wave transition in 2H-NbSe2 in real space. *Phys. Rev. B* **89,** 235115 (2014).

2. Soumyanarayanan, A. *et al.* Quantum phase transition from triangular to stripe charge order in NbSe$_2$. *Proc. Natl. Acad. Sci.* **110,** 1623–1627 (2013).

3. Bampoulis, P. *et al.* Defect Dominated Charge Transport and Fermi Level Pinning in MoS2/Metal Contacts. *ACS Appl. Mater. Interfaces* **9,** 19278–19286 (2017).

4. Rahnejat, K. C. *et al.* Charge density waves in the graphene sheets of the superconductor CaC_6. *Nat. Commun.* **2,** 558 (2011).